Journal of Alloys and Compounds 1071 (2026) 188901

Contents lists available at ScienceDirect

Journal of Alloys and Compounds

journal homepage: www.elsevier.com/locate/jalcom

Critical vanadium threshold for precipitation strengthening in ductile CoCrNiV alloys

Yusha Luo [a,b], Qihan Zheng [a,b], Ruixin Sheng [a,b], Qianqian Wang [a,b,*], Zhijun Guo [a,b,*], Baolong Shen [a,b]

[a] School of Materials Science and Engineering, Jiangsu Key Laboratory for Advanced Metallic Materials, Southeast University, Nanjing 211189, China
[b] Ministry of Education Key Laboratory of Structure and Thermal Protection for High-Speed Aircraft, Southeast University, Nanjing 211189, China

ARTICLE INFO

Keywords:
Multi-principal element alloys
Vanadium-induced precipitates strengthening
Mechanical property
Critical vanadium threshold

ABSTRACT

CoCrNi medium-entropy alloy exhibits excellent ductility, but its relatively low strength at room temperature limits its practical application in high-performance structural components. In this study, a series of as-cast $CoCrNiV_x$ (x = 0, 0.1, 0.3, and 0.5) multi-principal element alloys (MPEAs) were fabricated using high-vacuum arc melting to investigate the effects of vanadium (V) concentration on the microstructural evolution and mechanical properties of the CoCrNi-based system. A critical alloying threshold was identified at V0.3 alloy, marking a phase transformation from a single-phase FCC phase to a dual-phase structure containing BCC precipitates. The addition of V led to the enhanced mechanical properties, with the yield strength and Vickers hardness increased from 247 ± 2.5 MPa and 202 ± 4.6 HV in CoCrNi alloy to 460 ± 9.8 MPa and 288 ± 47.5 HV in $CoCrNiV_{0.5}$ alloy. However, the $CoCrNiV_{0.5}$ alloy exhibits a catastrophic ductile-to-brittle transition. This embrittlement is mechanistically attributed to the morphological evolution of BCC precipitates from discrete globules intragranularly to continuous networks along the grain boundaries, reducing elongation from 70% to 13%. The results show that precise control of the position of the precipitated phase is crucial for obtaining high properties as-cast CoCrNi-based alloys with synergistic strength and ductility at room temperature.

1. Introduction

The synergistic combination of high yield strength and exceptional ductility is highly desirable for ensuring the structural integrity of critical engineering components such as high-performance shafts and high-strength fasteners [1–3]. However, conventional alloy design is constrained by the inverse relationship between strength and ductility known as the strength-ductility trade-off [4]. This inherent limitation restricts the simultaneous optimization of mechanical properties in traditional alloy systems. The emergence of MPEAs has provided new strategies for addressing this strength-ductility conflict [5–7]. MPEAs differ from conventional alloys by consisting of five or more instead of one or two major elements with an equimolar or near-equimolar ratio. HEAs have attracted massive research because of their unique compositions, microstructures, and tunable properties. Among the various MPEAs, the CoCrFeMnNi alloy possesses good mechanical properties at both room and cryogenic temperatures [8,9]. The CoCrNi alloy exhibits superior mechanical properties compared to the CoCrFeMnNi alloy, including superior yield strength, higher ultimate tensile strength, and better ductility. The alloys possess a significantly lower stacking fault energy (SFE). Lower SFE facilitates the activation of deformation twinning (TWIP) during plastic deformation, endowing the alloys with exceptional work-hardening capacity and fracture toughness [10–12]. Despite the exceptional plasticity of the alloys, their insufficient yield strength limits their application, and it is significant to improve their strength and hardness at room temperature.

In order to further improve the yield strength of CoCrNi alloy, researchers achieve solid solution strengthening by adding other alloying elements. For instance, the addition of elements such as Ti [13], W [14], Al [15], Mo [16], and others to the alloys can significantly improve the mechanical properties of the alloys. Chang et al. [13] found that adding Ti to CoCrNi alloys increased hardness and strength through various mechanisms, such as solid solution strengthening, grain refinement, and precipitation hardening. Agustianingrum et al. [17] added Al in CoCrNi

* Corresponding authors at: School of Materials Science and Engineering, Jiangsu Key Laboratory for Advanced Metallic Materials, Southeast University, Nanjing 211189, China.
E-mail addresses: qwang678@seu.edu.cn (Q. Wang), zj-guo@seu.edu.cn (Z. Guo).

https://doi.org/10.1016/j.jallcom.2026.188901
Received 13 April 2026; Received in revised form 20 May 2026; Accepted 25 May 2026
Available online 26 May 2026

alloys to improve strength and concluded that the strength enhancement of the alloy was achieved through solid solution strengthening. Compared to the CoCrNi alloy, the $(CoCrNi)_{93}Al_7$ alloy exhibited an increased yield strength from 250 to 305 MPa and an improved ultimate tensile strength from 759 to 795 MPa, and its ultimate elongation remained at 68%. Lattice distortion has become one of the primary methods for enhancing the mechanical properties of MPEAs [18–26]. However, these strengthening strategies rely on complex mechanical processing, including cold rolling and annealing. These processes incur high manufacturing costs and long processing times. Consequently, it is necessary to study the direct development of high-strength MPEAs.

The V element was considered the most effective strengthening element for both FCC and BCC MPEAs due to its unique atomic volume [27–33], which created a significant mismatch with other primary elements. While the atomic radius of V is larger than the atomic radii of Co, Cr, and Ni, severe lattice distortion is expected upon the substitutional solid solution. During solidification, V exhibits a high tendency for micro-segregation within the liquid phase [3,34]. Chen et al. [25] prepared a $(CrCoNi)_{96}V_4$ alloy and, through cold rolling and annealing, increased its yield strength and tensile strength to 678 MPa and 1024 MPa, respectively, while maintaining an elongation of 26%. The addition of the V element has an obvious strengthening effect on the CrCoNi alloys.

In this study, we investigate as-cast $CoCrNiV_x$ alloys with different V contents (x = 0, 0.1, 0.3, and 0.5). The microstructure and mechanical properties of these as-cast alloys are examined. The alloys show a combination of good ductility and increased strength. This behavior comes from the high dislocation density inside the grains and the formation of precipitates. These results provide guidance for the processing and deformation of MPEAs that contain V.

2. Materials and methods

Alloy ingots with nominal compositions of $CoCrNiV_x$ MPEAs (x = 0, 0.1, 0.3, and 0.5, named as V0, V0.1, V0.3, and V0.5) were fabricated by arc-melting the mixtures of the high-purity (99.99 wt%) metals with a Ti getter under a vacuum of 5×10^{-3} Pa. Under this atmosphere, V may attract residual oxygen in the chamber, leading to the formation of interstitial oxygen-strengthened precipitates. The ingots of these multiprincipal element alloys were flipped and remelted at least five times to ensure homogeneity of compositions. Oxygen contamination was controlled through high-purity raw materials (99.99 wt%), Ti-getter purified argon, and high-vacuum conditions ($< 5 \times 10^{-3}$ Pa) during melting. This processing condition effectively controls interstitial oxygen content, although trace oxygen pickup is inevitable due to vanadium's high oxygen affinity. Dog-bone-shaped tensile specimens with a gauge length of 10 mm, a width of 2.5 mm, and a thickness of 1 mm were cut from the ingots using EDM. Tensile tests were carried out at room temperature utilizing a universal testing machine (MTS CMT-5105) to evaluate the mechanical properties of the samples at a strain rate of 1×10^{-3}. Three independent tensile tests were performed for every MPEA to ensure reproducibility. Vickers hardness was measured under a load of 300 g with a dwell time of 10 s, with a minimum of 10 indentations per sample. All samples were ground with SiC paper up to 2000 grit and polished using 0.04 μm SiO_2 suspensions to achieve a mirror-like surface morphology devoid of observable scratches under optical microscopy. Lastly, the samples were rinsed with deionized water after ultrasonic cleaning with acetone and ethanol.

Phase identifications were performed by X-ray diffraction (D8 Discover, Bruker, Germany) using 1.54 Å Cu-Kα radiation and scattering angle in the range of 20° to 100°. The microstructure analysis of the samples was carried out using a scanning electron microscope (SEM, Sirion) equipped with integrated Energy Dispersive Spectroscopy (EDS) and Electron Backscatter Diffraction (EBSD). Additionally, transmission electron microscopy (TEM, Talos F200X) was utilized to examine the interface structure and phase distribution of the samples. Sample preparation for TEM analysis involved the use of an ion milling machine (Gatan-691). Samples for TEM characterization were further mechanically ground with SiC papers down to a thickness of 60 μm, and then thinned by ion beam thinner (M691, GATAN, USA). The Vickers hardness of samples was measured using an automatic tester (FM-700, FUTURE-TECH, Japan) with a load of 300 g and a loading time of 10 s.

3. Results and discussion

3.1. Crystal structure and microstructures

The phase constitution of the as-cast $CoCrNiV_x$ alloys (x = 0, 0.1, 0.3, and 0.5) was characterized by X-ray diffraction (XRD). As illustrated in Fig. 1, all compositions display a single-phase face-centered cubic (FCC) crystal structure [16]. No additional peaks were detected [25]. An increasing V concentration triggers the nucleation of nanoscale BCC precipitates, which are nanoscale and present in relatively low volume fractions, which fall below the detection limit of XRD [35,36].

EBSD was adopted to measure the grain size of $CoCrNiV_x$ MPEAs. The inverse pole figure (IPF) mappings are shown in Fig. 2, which reveal a random distribution of crystallographic orientations for all alloys, evidenced by the various coloration of the grains. Notably, the grain size decreased with the increasing V content in the alloy. The V0 alloy is characterized by a coarse-grained microstructure with an average grain diameter (d_{mean}) of approximately 318 μm. The addition of V results in a slight refinement effect, with d_{mean} values of 248 μm and 247 μm, respectively (V0.1 and V0.3 alloy). Although the average grain size decreases to 174 μm, a sharp microstructural transition is adverse in the V0.5 alloy. The microstructure of the as-cast V0 alloy is shown in Fig. 3, which indicates a classical low stacking fault energy (SFE) material [37]. Bright-field TEM imaging (Fig. 3a) demonstrates a clean matrix devoid of any secondary phase particles, either at the grain boundaries or within the grain interiors. The matrix contains a few dislocations and stacking faults (SFs). In the illustration, the selected area electron diffraction (SAED) patterns confirm the single-phase constitution. High-resolution TEM (HRTEM) analysis (Figs. 3b, 3c) reveals a high density of SFs traversing the FCC matrix, confirmed by the characteristic streaking in the Fast Fourier Transform (FFT) patterns. This abundance of thermally induced defects in the as-cast state serves as direct evidence of the low intrinsic SFE of the CoCrNi system [38,39].

The V0.1 alloy maintains a single-phase FCC structure. As shown in Fig. 3d, it exhibits a homogeneous microstructure similar to the V0 alloy. It is characterized by a low initial dislocation density. However, an

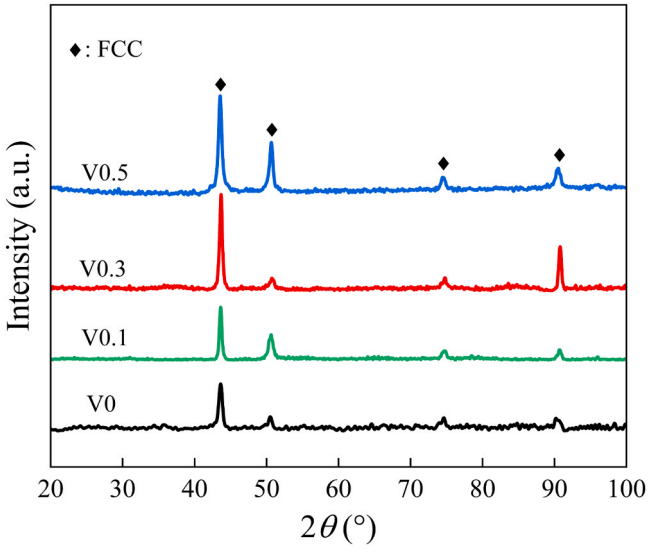

Fig. 1. XRD patterns of the $CoCrNiV_x$ (x = 0, 0.1, 0.3, and 0.5) alloys.

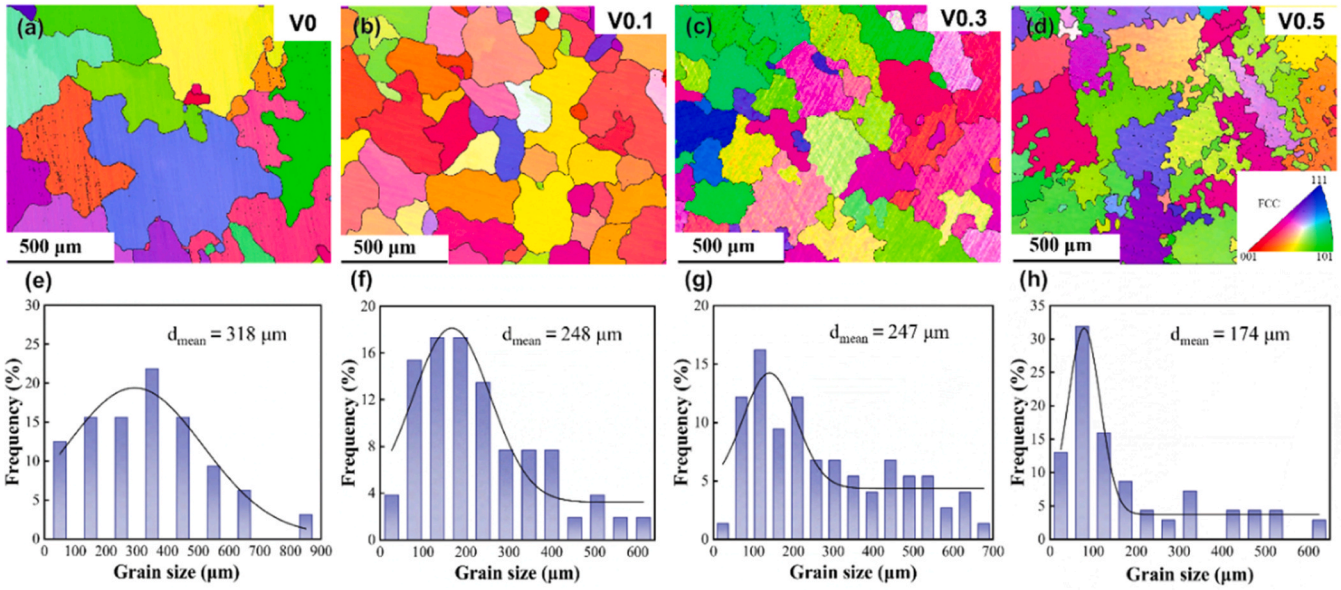

Fig. 2. EBSD IPF mappings and the distribution of grain sizes in $CoCrNiV_x$ alloys (a, e) V0, (b, f) V0.1, (c, g) V0.3, and (d, h) V0.5.

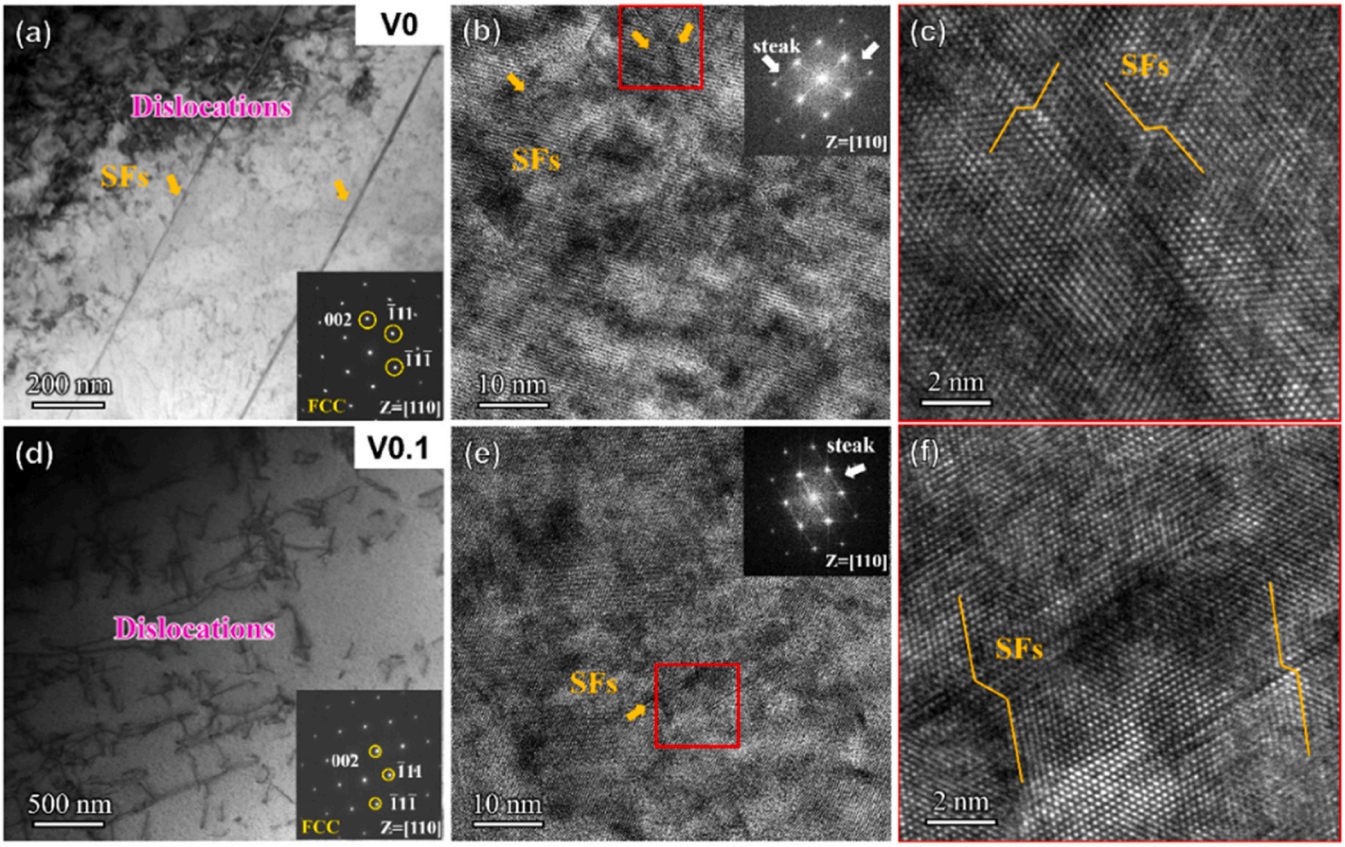

Fig. 3. The microstructure of as-cast V0 and V0.1 alloys. (a, d) TEM BF images of V0 and V0.1 and (b, e) HRTEM of V0 and V0.1; (c, f) an enlarged view of SFs marked by the red square in Figs. (b) and (e), respectively.

obvious difference was observed in the SFs behavior. The number of SFs in the V0.1 alloy is significantly lower than that in the V0 alloy. The V0 alloy exhibits SFs along multiple directions, while only a single direction is observed in the V0.1 alloy (Figs. 3e and 3f). The V0.3 alloy marks a critical microstructural threshold characterized by the appearance of intragranular precipitation. As shown in Fig. 4b, globular precipitates are densely distributed within the grain interiors. EDS mapping (Fig. 4b) confirms that these intragranular globular phases are enriched in V and O, while being depleted in the matrix elements (Co, Cr, Ni). The interface between these nanoscale precipitates and the matrix exhibits dislocation pinning (Fig. 4c), suggesting an obstacle effect against dislocation slip. Structural analysis via SAED (Fig. 4d-f) identifies that

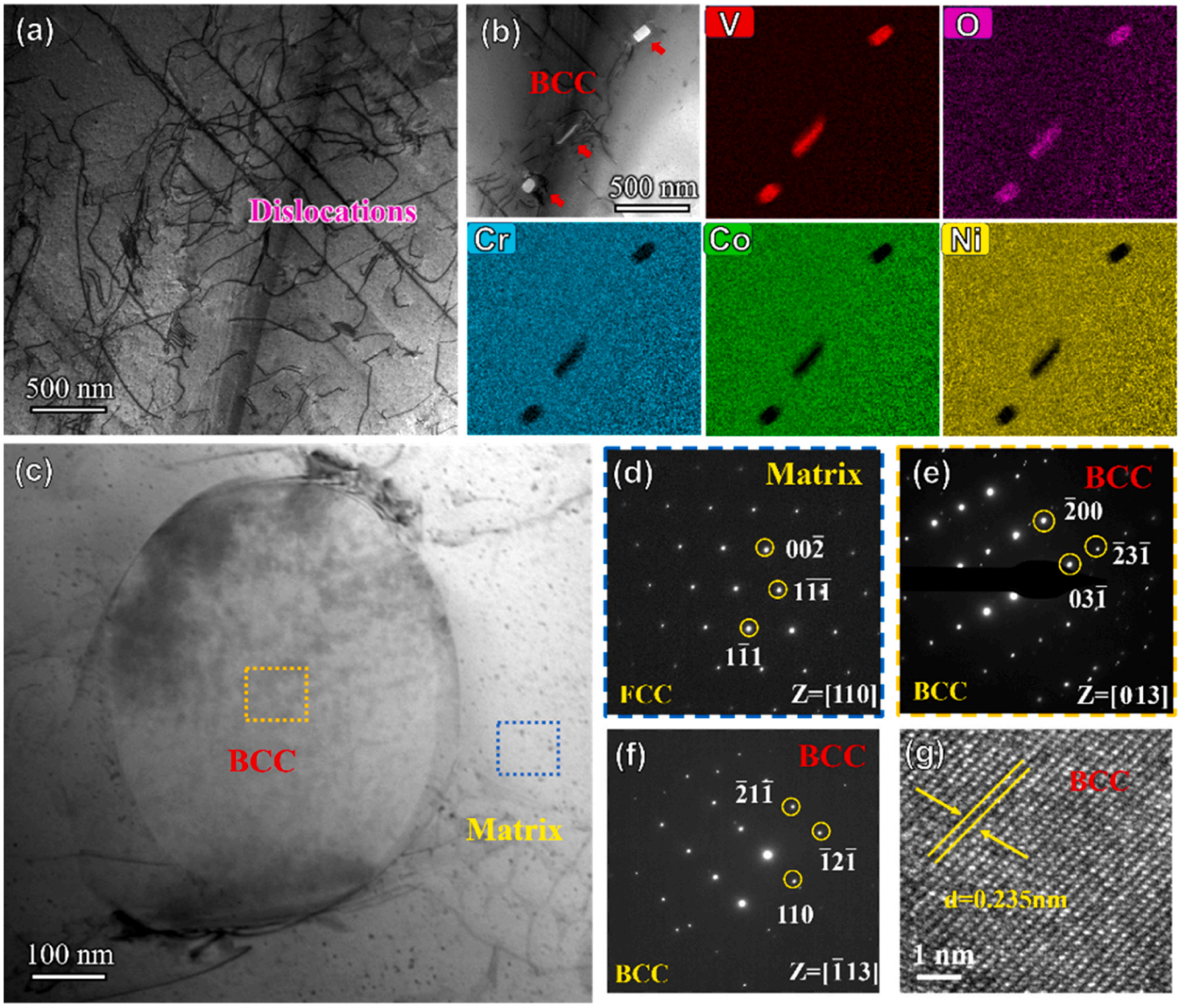

Fig. 4. The microstructure of as-cast V0.3 alloy. (a) BF image; (b) BF image with EDS plots of V0.3 alloy; (c) BF images of BCC precipitate; (d-f) SAED patterns of matrix and BCC precipitate; (g) HRTEM image of the BCC precipitate.

the matrix remains FCC structure, while these internal particles have a BCC crystal structure along the [013] and [113] zone axis. The HRTEM image (Fig. 4g) reveals clear lattice fringes with an interplanar spacing of d = 0.235 nm.

With the V content increasing to 0.5, the microstructure of the alloy changes significantly. In Fig. 5a, the bright-field TEM image shows the grain boundary (GB) of V0.5 alloy. The BCC precipitates (indicated by red arrows) are continuously distributed adjacent to the grain boundaries. The massive segregation of V into these precipitates leads to a localized V-depleted zone in the adjacent matrix. This causes the surrounding matrix (marked by the blue dashed box in Fig. 5a) to become relatively enriched in the Cr element. Fig. 5b shows the SAED patterns that the distribution of diffraction spots confirms that this localized Cr-enriched matrix strictly maintains the standard FCC structure. The EDS elemental mapping reveals pronounced enrichment of V and O at the grain boundaries. The projected one-dimensional concentration profiles along the green arrows (Fig. 5c) provide a semi-quantitative analysis of elemental partitioning. V and O, accounting for over 65% of the total composition, preferentially segregate to the grain-boundary precipitates, whereas Cr, at nearly 40%, is predominantly enriched in the left-side precipitate. The FCC matrix exhibits a largely uniform elemental distribution, indicating a segregation-controlled precipitation pathway. Fig. 5d further illustrates the overall distribution of BCC precipitates at multiple grain boundaries. This observation confirms the universality of the local phenomenon shown in Fig. 5a. Fig. 5e presents the image of the interface between the BCC precipitates and the matrix, and the SAED pattern confirmed the BCC structure. Fig. 5f presents a high-resolution TEM image of the interface. It is evident that when the atomic lattice on the side of the precipitate is clear, the lattice of the matrix would become ambiguous, revealing different lattice arrangements and incoherent correlation between the precipitate and matrix [40].

To quantitatively evaluate the microstructural evolution across the critical threshold, statistical analysis was conducted on multiple bright-field TEM and SEM images. In the V0.3 alloy, discrete intragranular BCC precipitates exhibit an average equivalent diameter of 193.5 ± 63.0 nm, with an area fraction of 0.03%. And no precipitates were observed at the grain boundaries in the V0.3 alloy. In contrast, the V0.5 alloy displays a significant morphological transition; the precipitates coarsen to 234.2 ± 82.8 nm, while the area fraction and number density reach 0.15%. These precipitates exhibit preferential segregation toward grain boundaries, reaching a grain-boundary coverage of 24%.

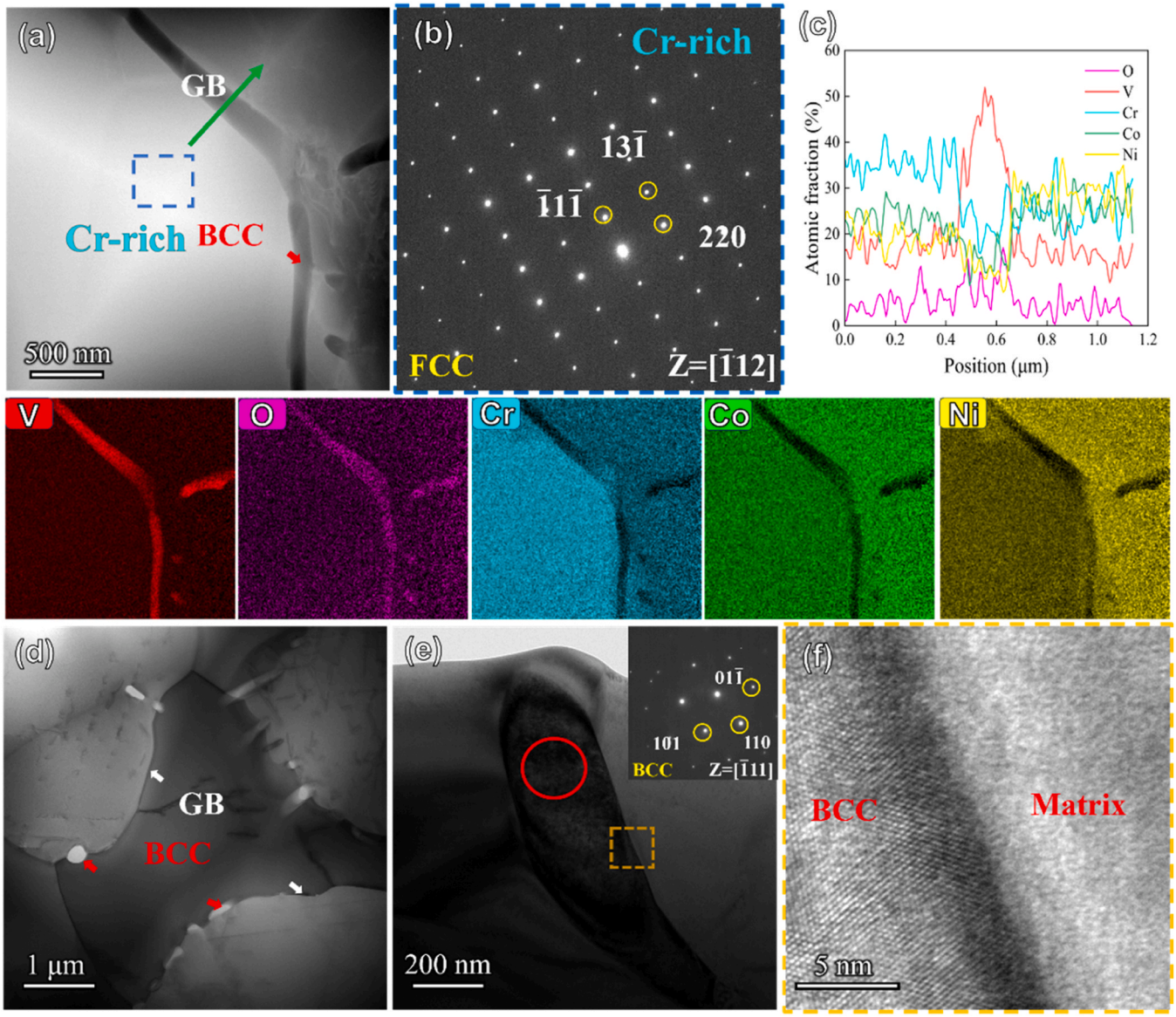

Fig. 5. The microstructure of as-cast V0.5 alloy. (a) HAADF image with EDS plots of V0.5 alloy, EDS mapping analysis indicating BCC precipitate in matrix; (b) SAED pattern of Cr-rich precipitate; (c) The projected one-dimensional concentration profiles along the green arrows in (a); (d) BF images of V0.5 alloy; (e) STEM image of precipitate; (f) high resolution image confirms the incoherent relationship between the BCC precipitate and matrix.

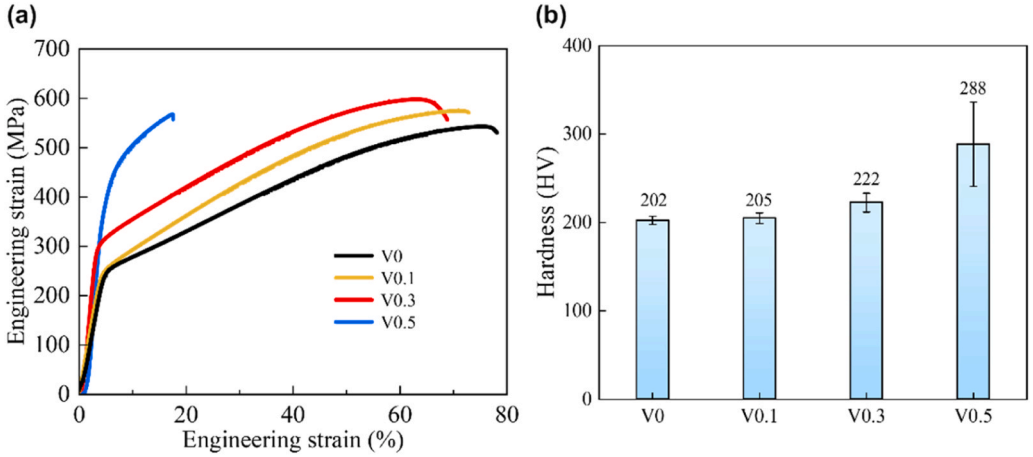

Fig. 6. Mechanical properties of CoCrNiV$_x$ MPEAs. (a) Engineering stress-strain curves and (b) hardness.

3.2. Mechanical properties

As research demonstrates, alloy microstructure directly influences strength, toughness, elastic modulus, and plasticity. Mechanical properties of the $CoCrNiV_x$ alloys were obtained using tensile tests and microhardness measurements. Fig. 6(a) shows the engineering stress-strain curves of the V0, V0.1, V0.3, and V0.5 alloys. The V0 alloy achieves a yield strength of 247 ± 2.5 MPa and a tensile strength of 540 ± 6.7 MPa, and its ductility remains 70%. The tensile strength and ductility both improve in the V0.1 alloy. As the V content further increases to the V0.3 alloy, the yield strength reaches 298 ± 6.1 MPa without sacrificing ductility. When the V content further increases to the V0.5 alloy, the yield strength reaches 460 ± 9.8 MPa, but the ductility drops to 13%. The morphological transition of the BCC precipitates, from dispersed spherical precipitates to grain boundary-aligned strip-shaped, creates interfacial mechanical property disparities due to compositional disparity with the FCC matrix. These disparities generate localized back stresses that hinder dislocation motion, enhancing yield strength [41–43]. During plastic deformation, the BCC precipitates at the grain boundary in the V0.5 alloy promote dislocation pile-up at interfaces, initiating localized stress concentration. This micromechanical response facilitates premature crack nucleation and propagation through weakened grain boundaries, degrading ductility and inducing brittle fracture.

A microhardness tester was used to measure the Vickers hardness of alloys. At least 10 tests were conducted for each alloy, using a loading force of 0.5 kg and a holding time of 10 s. Hardness testing is closely related to its yield strength. The hardness of the alloys was measured using a microhardness tester, as depicted in Fig. 6(b). It can be observed that the overall hardness of the alloy increases with increasing V content. The hardness of the V0 is 202 ± 4.6 HV, while the hardness of V0.1 and V0.3 alloys gradually increases to 205 ± 6.1 HV and 222 ± 10.6 HV, reflecting the strengthening effect observed in macroscopic tensile tests.

This increase is mainly attributed to solid solution strengthening (V0.1 alloy), followed by enhancement through effective nanoscale precipitate hardening (V0.3 alloy), which is confirmed by TEM results in Fig. 3, Fig. 4, and Fig. 5. The V0.5 alloy achieves the highest hardness of 288 ± 47.5 HV. This increment is disproportionate compared to the transition from V0.1 to V0.3. This escalation is attributed to the high volume fraction and specific morphology of the BCC precipitates. From a structural perspective, these BCC-structured precipitates possess intrinsically higher resistance to dislocation motion compared to the ductile FCC matrix. As the microstructure evolves from discrete particles to a continuous, hard BCC network (as shown in Fig. 5), which constricts plastic deformation during indentation, thereby leading to the increase in Vickers hardness.

3.3. Deformation mechanisms

The systematic variation in V content induces an interplay between SFE, precipitation, and deformation mechanisms. To unveil the fracture mechanisms of the alloy systems, the fracture surface morphologies of as-cast $CoCrNiV_x$ MPEAs (x = 0, 0.1, 0.3, and 0.5) are displayed in Fig. 7, where Fig. 7(e)–(h) represent the high-magnification views of the specific regions identified in Fig. 7(a)–(d), respectively. For the V0, V0.1, and V0.3 alloys, the fracture surfaces are characterized by a high density of large and deep dimples (Fig. 7a–c) and their corresponding enlarged views in Fig. 7(e)–(g). These features are classified as the typical ductile fracture. The deep dimples suggest that the matrix possesses strain-hardening capacity [44]. This observation is consistent with the exceptional uniform elongation of ~70% maintained by these alloys. In contrast, a microstructural and mechanical transition is observed as the V content reaches the V0.5 alloy. The fracture surface of the V0.5 alloy, displayed in Fig. 7(d, h), transforms a brittle fracture morphology characterized by cleavage facets. Consequently, a feature of the ductile-to-brittle transition is observed with increasing V content, correlating with the decline in ductility to 13%. The mechanistic origin of this embrittlement in V0.5 alloy is traced to the morphological evolution of the BCC phases from discrete globules into continuous, film-like networks along the grain boundaries. The results of the fracture surface morphologies of these four alloy regimes were consistent with the corresponding tensile properties shown in Fig. 6. [45,46].

Post-deformation microstructural characterization in Fig. 8(a) and (b) reveals that the V0 alloy undergoes significant deformation twinning. The formation of nanoscale deformation twins facilitates plastic strain accommodation while simultaneously partitioning the grain interiors into refined structural domains [47,48]. The high density of coherent twin boundaries acts as effective planar obstacles that impede dislocation motion, thereby promoting dislocation accumulation and interactions at these interfaces. This dynamic evolution of the internal microstructure sustains a high strain-hardening rate throughout the deformation process, effectively suppressing the onset of plastic instability. Consequently, the robust hardening behavior enabled by these

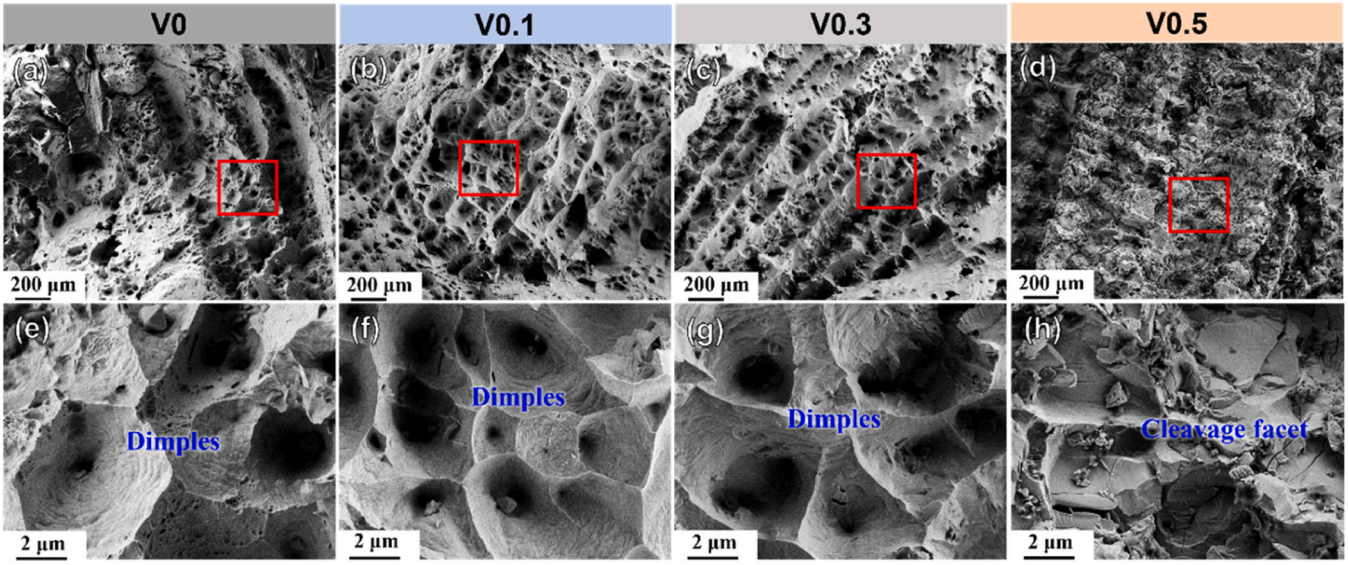

Fig. 7. The SEM images showing the fracture surface morphologies of (a, e) V0, (b, f) V0.1, (c, g) V0.3, and (d, h) V0.5 alloys.

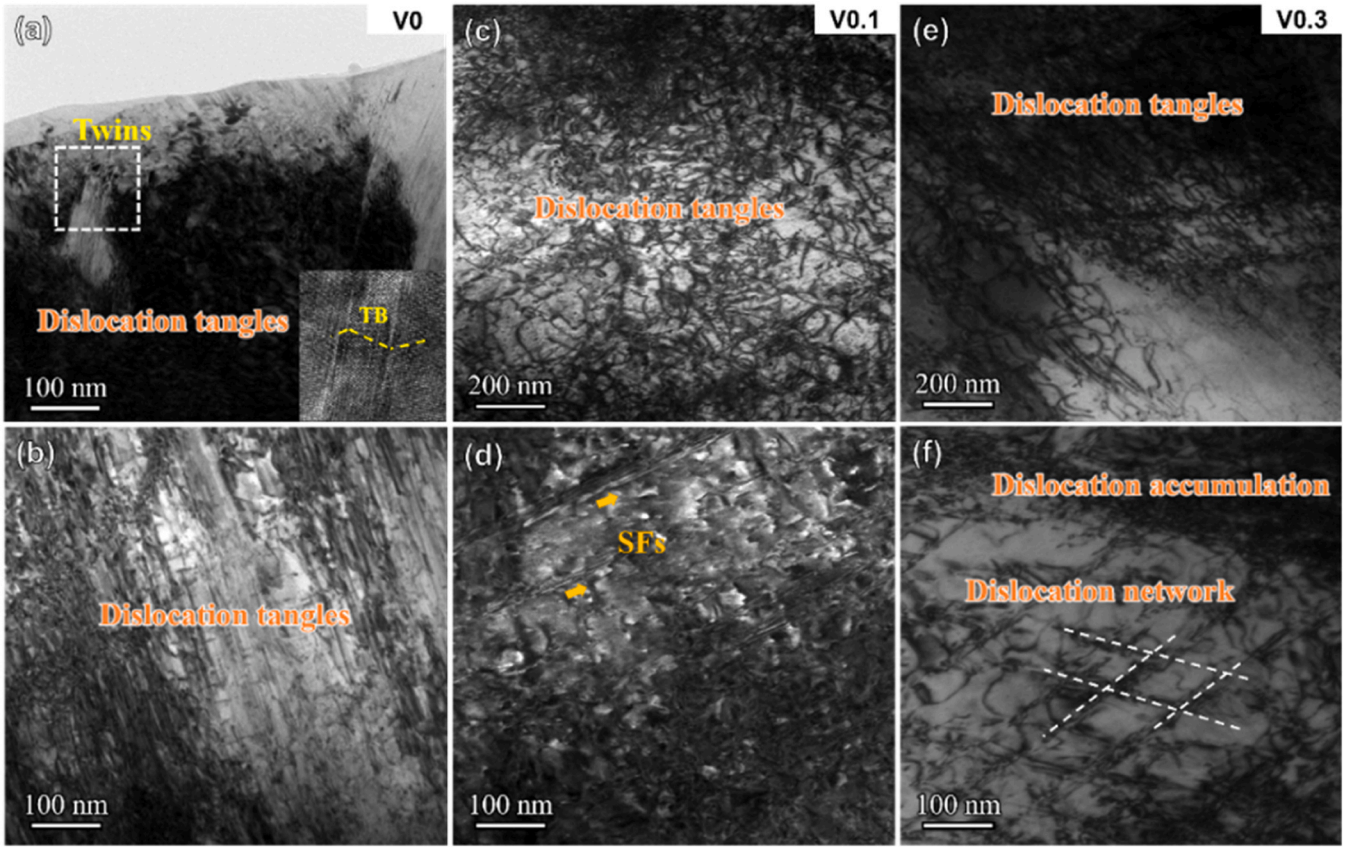

Fig. 8. Deformation mechanisms of the V0, V0.1, and V0.3 alloys. (a-b) Dislocation tangles and DTs in V0 alloy; (c-d) Dislocation tangles and SFs in V0.1 alloy; (e-f) Dislocation tangles and networks in V0.3 alloy.

twin boundaries accounts for the exceptional ductility (~70%) exhibited by the V0 alloy. Fig. 8(c) and (d) illustrate the post-deformation microstructure of the V0.1 alloy. In contrast to its initial state, the deformed matrix exhibits dislocation proliferation, characterized by high-density accumulation and intricate entanglements. This dislocation-induced hardening constitutes the primary contribution to the observed yield strength enhancement and sustained work-hardening response. Fig. 8(c) shows the presence of isolated SFs embedded within the dense dislocation networks. This observation stands in contrast to the deformed V0 base alloy (Fig. 8(a)), where mechanical twinning serves as the deformation mode. Notably, no discernible mechanical twins were observed in the strained V0.1 alloy. This mechanistic shift suggests that the addition of V slightly elevates the SFE or increases the critical resolved shear stress required for twin nucleation [49]. Consequently, the alloy facilitates dislocation slip as the primary carrier of plasticity under the given loading conditions. Although the TWIP effect appears suppressed, the efficient dislocation multiplication and hardening maintain an obvious strain-hardening rate, thereby rationalizing the uniform retained in the V0.1 alloy (Fig. 6). The refinement of grain size in the V0.1 alloy compared to the base V0 alloy can be attributed to the solute drag effect. Although the V0.1 alloy maintains a single-phase FCC structure without precipitation, the V atoms tend to segregate at the moving grain boundaries during solidification and cooling [50]. The presence of these solute atoms exerts a dragging force that thermodynamically restricts grain boundary migration. Thus, they can suppress grain growth even in the absence of precipitate pinning [51].

From a micromechanical perspective, the interaction between mobile dislocations and these hard BCC-structured precipitates is governed by the Orowan mechanism [52]. As dislocations encounter these hard BCC particles, they are unable to shear through them; instead, they are forced to bow between the obstacles, eventually leaving behind Orowan loops. Each looping increases the back-stress exerted on subsequent dislocations, thereby providing a strengthening component to the lattice [53]. A factor in maintaining the ductility of the V0.3 alloy is the spatial distribution and morphology of these BCC precipitates. Unlike the continuous films observed in V0.5, the precipitates in V0.3 are globular and discontinuously distributed within the grains. This discrete morphology ensures the ductility of the V0.3 alloy. Furthermore, the strategic modulation of the matrix SFE through V addition plays a dual role. It not only suppresses mechanical twinning but also enhances the chemical and structural stability of the FCC phase. By elevating the SFE, V suppresses such brittle phase transformations, ensuring that the matrix deforms solely through the evolution of dislocation substructures, such as cells and walls. This intricate cooperation, where the nanoscale precipitates provide the high initial stress and the matrix provides the necessary strain hardenability, constitutes the core synergy responsible for the superior performance and damage tolerance of the V0.3 alloy.

Post-deformed TEM micrographs of V0.5 alloy provide evidence of interaction between dislocations and precipitated phases. In Fig. 9(a), the large precipitated phase is a barrier to dislocation slip in the FCC matrix. The dense dislocation accumulation at the phase boundary indicates that these precipitates are not shearable, forcing the dislocation to accumulate and tangle at the phase boundary. This blockage increases the local back stress and contributes to an increase in yield strength through the Orowan bypass mechanism [54]. Also, Fig. 9(b) illustrates the micromechanics response at the GB. An obvious accumulation of dislocations was observed near the precipitate beside GB, highlighting the constraint of plastic strain between adjacent grains. The local accumulation of such defects results in large stress concentrations at the interface. In Fig. 9(c-d), cracks nucleate preferentially at the precipitates along the grain boundaries. Due to the inherent brittleness of these coarse precipitates and their significant elastic mismatch with the

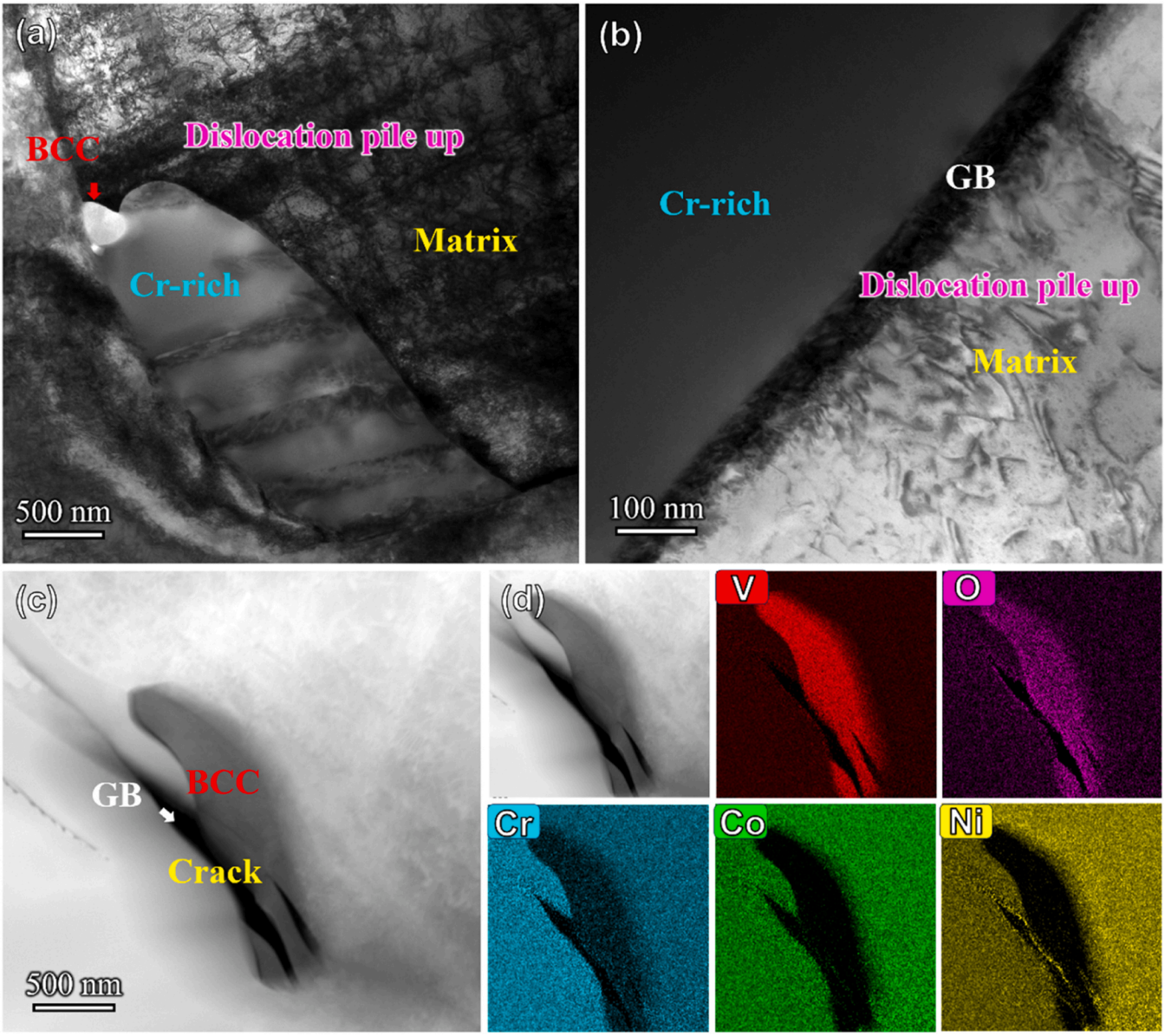

Fig. 9. The deformation mechanism of V0.5 alloy. (a) Dislocation pile-ups around the precipitation; (b) Dislocation pile-ups at GB; (c) HADDF image of the crack of precipitation; (d) EDS mappings of the crack.

ductile matrix, these precipitates are the primary triggers for microcrack initiation.

The failure of the V0.5 alloy illustrates the negative consequences of exceeding the alloying threshold in MPEAs. The primary cause of embrittlement is the morphological transition of the second phase from discrete and globular particles to a continuous morphology along the grain boundaries (Fig. 5). Such continuous grain-boundary phases are known to severely degrade ductility in MPEAs [55]. The coarse elongated BCC precipitates at the grain boundaries act as severe stress concentrators. Due to their inherent brittleness and incoherency with the matrix, these phases cannot accommodate the strain compatibility requirements during tensile loading [56]. Consequently, microcracks nucleate internally within these particles or at the particle/matrix interface at very low macroscopic strains (~18%) [57].

These microcracks find a continuous, low-resistance propagation path along the brittle grain boundary network. This phenomenon bypasses or compromises the intrinsic toughening mechanisms of the ductile FCC matrix [58]. The crack tip propagates rapidly through the interconnected brittle network, largely avoiding the grain interiors where plastic energy dissipation via dislocation slip would typically occur. This process, termed intergranular fracture assisted by continuous secondary phases, accounts for the catastrophic loss of macroscopic toughness and the emergence of quasi-cleavage features in the fractography [59]. Although the interconnected hard precipitates provide high resistance to indentation, it lacks the essential damage tolerance required to sustain tensile ductility.

The Phase stability of the $CoCrNiV_x$ MPEAs can be further understood through the valence electron concentration (VEC) criterion. The VEC of the present alloys is calculated by

$$\mathrm{VEC} = \sum_{i=1}^{n} c_i \, (VEC)_i \tag{1}$$

where c_i and $(VEC)_i$ are the atomic percentage and the valence electron concentration of the i element, respectively. The calculated VEC values for x = 0, 0.1, 0.3, and 0.5 are 8.33, 8.23, 8.03, and 7.86, respectively. According to the criterion proposed by Guo et al. [60], an FCC phase is stable when VEC $\geq$ 8.0, while a dual-phase (FCC+BCC) region exists when 6.87 $\leq$ VEC $<$ 8.0. The decrease in VEC with increasing V

concentration explains the observed phase transition. For the V0.3 alloy, the VEC value (8.03) is approaching 8.0, which corresponds with the experimental observation of the initial precipitation of the BCC phase.

By exploiting the natural tendency of elements like V to segregate, one can induce precipitation strengthening in the as-cast state, bypassing the need for energy-intensive thermomechanical treatments (rolling + aging) typical of traditional superalloys. However, this window is narrow. The findings establish that the success of this strategy relies on keeping the solute content below the threshold of continuous film formation ($x < 0.5$) while high enough to ensure sufficient precipitate density ($x = 0.3$). The V0.3 alloy exemplifies the successful execution of this philosophy, offering a viable pathway for producing high-strength and high-ductility MPEAs for structural applications.

4. Conclusion

A series of $CoCrNiV_x$ ($x = 0$, 0.1, 0.3, and 0.5) MPEAs was processed using high-vacuum arc melting to study the effects of V additions on microstructures and mechanical properties of the MPEAs, and the following could be concluded. It was found that both the hardness and tensile strength increased, but the fracture elongation decreased with V additions. The strengthening mechanisms were mainly attributed to solid solution strengthening, grain refinement, and precipitation strengthening. The morphologies of tensile fracture surfaces showed the ductile-to-brittle transition with the increasing V content. In the V0.3 alloy, a synergistic architecture consisting of a ductile FCC matrix and nanoscale BCC precipitates was achieved. The precipitates are prone to occur at grain boundaries and within the matrix, acting as potent obstacles to dislocation motion. However, further increasing the V content to V0.5 results in a transition where these precipitates evolve from discrete globules into an interconnected brittle network. The V0.3 alloy exhibits a superior yield strength and still retains an exceptional level of plasticity. This work proves that the design of such heterogeneous microstructures is an effective strategy for significantly enhancing the strength of FCC MPEAs while retaining a certain degree of plasticity.

CRediT authorship contribution statement

Yusha Luo: Writing – original draft, Visualization, Methodology, Formal analysis. **Ruixin Sheng:** Formal analysis, Data curation. **Qihan Zheng:** Writing – original draft, Investigation, Formal analysis, Data curation. **Zhijun Guo:** Supervision, Resources, Project administration. **Qianqian Wang:** Writing – review & editing, Supervision, Funding acquisition, Conceptualization. **Baolong Shen:** Supervision, Resources, Project administration, Funding acquisition.

Declaration of Competing Interest

The authors declare that they have no known competing financial interests or personal relationships that could have appeared to influence the work reported in this paper.

Acknowledgments

This work was supported by the National Natural Science Foundation of China (52231005, 52571183).

References

[1] J.W. Morris, Maraging steels: making steel strong and cheap, Nat. Mater. 16 (2017) 787–789.
[2] J. Inoue, S. Nambu, Y. Ishimoto, T. Koseki, Fracture elongation of brittle/ductile multilayered steel composites with a strong interface, Scr. Mater. 59 (2008) 1055–1058.
[3] G. Salishchev, M. Tikhonovsky, D. Shaysultanov, N. Stepanov, A. Kuznetsov, I. Kolodiy, A. Tortika, O. Senkov, Effect of Mn and V on structure and mechanical properties of high-entropy alloys based on CoCrFeNi system, J. Alloy. Compd. 591 (2014) 11–21.
[4] R.O. Ritchie, The conflicts between strength and toughness, Nat. Mater. 10 (2011) 817–822.
[5] J.W. Yeh, S.K. Chen, S.J. Lin, J.Y. Gan, T.S. Chin, T.T. Shun, C.H. Tsau, S.Y. Chang, Nanostructured High-Entropy Alloys with Multiple Principal Elements: Novel Alloy Design Concepts and Outcomes, Adv. Eng. Mater. 6 (2004) 299–303.
[6] P. Huang, J. Yeh, T. Shun, S. Chen, Multi-principal-element alloys with improved oxidation and wear resistance for thermal spray coating, Adv. Eng. Mater. 6 (2004) 74–78.
[7] B. Cantor, I.T.H. Chang, P. Knight, A.J.B. Vincent, Microstructural development in equiatomic multicomponent alloys, Mater. Sci. Eng. A 375 (2004) 213–218.
[8] B. Gludovatz, A. Hohenwarter, D. Catoor, E.H. Chang, E.P. George, R.O. Ritchie, A fracture-resistant high-entropy alloy for cryogenic applications, Science 345 (2014) 1153–1158.
[9] F. Otto, A. Dlouhý, C. Somsen, H. Bei, G. Eggeler, E.P. George, The influences of temperature and microstructure on the tensile properties of a CoCrFeMnNi high-entropy alloy, Acta Mater. 61 (2013) 5743–5755.
[10] Z. Wu, H. Bei, G.M. Pharr, E.P. George, Temperature dependence of the mechanical properties of equiatomic solid solution alloys with face-centered cubic crystal structures, Acta Mater. 81 (2014) 428–441.
[11] Z. Wu, H. Bei, F. Otto, G.M. Pharr, E.P. George, Recovery, recrystallization, grain growth and phase stability of a family of FCC-structured multi-component equiatomic solid solution alloys, Intermetallics 46 (2014) 131–140.
[12] G. Laplanche, A. Kostka, C. Reinhart, J. Hunfeld, G. Eggeler, E.P. George, Reasons for the superior mechanical properties of medium-entropy CrCoNi compared to high-entropy CrMnFeCoNi, Acta Mater. 128 (2017) 292–303.
[13] W.-C. Chang, C.-H. Hsueh, Strengthening of CoCrNi medium entropy alloy with Ti additions, Intermetallics 163 (2023) 108072.
[14] R. Chang, W. Fang, X. Bai, C. Xia, X. Zhang, H. Yu, B. Liu, F. Yin, Effects of tungsten additions on the microstructure and mechanical properties of CoCrNi medium entropy alloys, J. Alloy. Compd. 790 (2019) 732–743.
[15] M. Agustianingrum, S. Yoshida, N. Tsuji, N. Park, Effect of aluminum addition on solid solution strengthening in CoCrNi medium-entropy alloy, J. Alloy. Compd. 781 (2019) 866–872.
[16] Q. Li, M. Wang, X. Wang, Y. Lu, T. Wang, Partially recrystallized heterostructure via Mo-doping endows CoCrNi medium-entropy alloy with exceptional strength and ductility, Scr. Mater. 253 (2024) 116297.
[17] R.B. Chang, W. Fang, H.Y. Yu, X. Bai, X. Zhang, B.X. Liu, F.X. Yin, Heterogeneous banded precipitation of $(CoCrNi)_{93}Mo_7$ medium entropy alloys towards strength-ductility synergy utilizing compositional inhomogeneity, Scr. Mater. 172 (2019) 144–148.
[18] H. Zhang, G. Sun, M. Yang, F. Yuan, X. Wu, Simultaneous improvement of strength and ductility in a P-doped CrCoNi medium-entropy alloy, J. Mater. Sci. Technol. 209 (2025) 128–138.
[19] D.D. Zhang, H. Wang, J.Y. Zhang, H. Xue, G. Liu, J. Sun, Achieving excellent strength-ductility synergy in twinned NiCoCr medium-entropy alloy via Al/Ta co-doping, J. Mater. Sci. Technol. 87 (2021) 184–195.
[20] I. Moravcik, V. Hornik, P. Minárik, L. Li, I. Dlouhy, M. Janovska, D. Raabe, Z. Li, Interstitial doping enhances the strength-ductility synergy in a CoCrNi medium entropy alloy, Mater. Sci. Eng. A 781 (2020) 139242.
[21] I. Moravcik, H. Hadraba, L. Li, I. Dlouhy, D. Raabe, Z. Li, Yield strength increase of a CoCrNi medium entropy alloy by interstitial nitrogen doping at maintained ductility, Scr. Mater. 178 (2020) 391–397.
[22] J. Yen, C. Hsueh, Effects of Ti and Mo additions on microstructures and mechanical properties of CoCrNi medium entropy alloys, Mater. Sci. Eng. A 926 (2025) 147943.
[23] Z. Sun, X. Tan, C. Wang, M. Descoins, D. Mangelinck, S.B. Tor, E.A. Jägle, S. Zaefferer, D. Raabe, Reducing hot tearing by grain boundary segregation engineering in additive manufacturing: example of an AlxCoCrFeNi high-entropy alloy, Acta Mater. 204 (2021) 116505.
[24] J.Y. He, H. Wang, H.L. Huang, X.D. Xu, M.W. Chen, Y. Wu, X.J. Liu, T.G. Nieh, K. An, Z.P. Lu, A precipitation-hardened high-entropy alloy with outstanding tensile properties, Acta Mater. 102 (2016) 187–196.
[25] J. Chen, Q. Lai, X. Zhao, J. Yi, Q. Li, Effect of room temperature rolling and annealing on microstructure and mechanical properties of $(CrCoNi)_{96}V_4$ medium entropy alloy, Intermetallics 174 (2024) 108468.
[26] X. Hong, C.-H. Hsueh, Effects of yttrium addition on microstructures and mechanical properties of CoCrNi medium entropy alloy, Intermetallics 140 (2022) 107405.
[27] B. Yin, F. Maresca, W. Curtin, Vanadium is an optimal element for strengthening in both fcc and bcc high-entropy alloys, Acta Mater. 188 (2020) 486–491.
[28] S.S. Sohn, A. Kwiatkowski da Silva, Y. Ikeda, F. Kormann, W. Lu, W.S. Choi, B. Gault, D. Ponge, J. Neugebauer, D. Raabe, Ultrastrong medium-entropy single-phase alloys designed via severe lattice distortion, Adv. Mater. 31 (2019) 1807142.
[29] R. Shen, Z. Ni, S. Peng, H. Yan, Y. Tian, Effects of V addition on the deformation mechanism and mechanical properties of non-equiatomic CoCrNi medium-entropy alloys, Materials 16 (2023) 5167.
[30] Z. Ni, Z. Li, R. Shen, S. Peng, H. Yan, Y. Tian, Achieving excellent strength-ductility balance in single-phase CoCrNiV multi-principal element alloy, Materials 16 (2023) 6530.
[31] Y.H. Jo, S. Jung, W.M. Choi, S.S. Sohn, H.S. Kim, B.J. Lee, N.J. Kim, S. Lee, Cryogenic strength improvement by utilizing room-temperature deformation twinning in a partially recrystallized VCrMnFeCoNi high-entropy alloy, Nat. Commun. 8 (2017) 15719.
[32] M. Hu, X. Jiang, M. Dong, M. Hu, Y. Yang, Preparation and effect of vanadium addition on the mechanical properties of CoCrFeNiVx high-entropy alloy, J. Mater. Res. Technol. 27 (2023) 7705–7712.

[33] W.-M. Choi, Y.H. Jo, D.G. Kim, S.S. Sohn, S. Lee, B.-J. Lee, A thermodynamic description of the Co-Cr-Fe-Ni-V system for high-entropy alloy design, Calphad 66 (2019) 101624.
[34] A. Fan, J. Li, M. Tsai, On the phase constituents of three CoCrFeNiX (X = V, Nb, Ta) high-entropy alloys after prolonged annealing, J. Alloy. Compd. 823 (2020) 153524.
[35] P. Zhang, C. Zhao, R. Wang, Y. Liu, Y. Chen, Study on Microstructural Evolution, Strengthening and Deformation Mechanisms of a CoCrNi-Based Medium-Entropy Alloy with Different Annealing Times, Materials 19 (2026) 945.
[36] H. Kim, D. Lee, D. Kwen, Y. Koo, E. Kim, H. Cho, H. Kim, Y. Kim, M. Jang, N. Park, B. Straumal, M. Agustianingrum, The Formation of B2-precipitate and its Effect on Grain Growth Behavior in Aluminum-containing CoCrNi Medium-entropy Alloy, Mater. Lett. 303 (2021) 130481.
[37] S. Zhao, S. Yin, X. Liang, F. Cao, Q. Yu, R. Zhang, L. Dai, C.J. Ruestes, R.O. Ritchie, A.M. Minor, Deformation and failure of the CrCoNi medium-entropy alloy subjected to extreme shock loading, Sci. Adv. 9 (2023) eadf8602.
[38] S. Zhao, G.M. Stocks, Y. Zhang, Stacking fault energies of face-centered cubic concentrated solid solution alloys, Acta Mater. 134 (2017) 334–345.
[39] I. Moravcik, M. Zelený, A. Dlouhy, H. Hadraba, L. Moravcikova-Gouvea, P. Papež, O. Fikar, I. Dlouhy, D. Raabe, Z. Li, Impact of interstitial elements on the stacking fault energy of an equiatomic CoCrNi medium entropy alloy: theory and experiments, Sci. Technol. Adv. Mater. 23 (2022) 376–392.
[40] F. Zhang, J. He, Y. Wu, H. Mao, H. Wang, X. Liu, S. Jiang, T.G. Nieh, Z. Lu, Effects of Ni and Al on precipitation behavior and mechanical properties of precipitation-hardened CoCrFeNi high-entropy alloys, Mater. Sci. Eng. A 839 (2022) 142879.
[41] E. Wang, J. Li, F. Kang, F. Jiang, L. Lv, B. Dai, Y. Cao, W. Jiang, Balancing the mechanical properties of $Al_{0.45}CoCrFeNiTi_x$ high-entropy alloys by tailoring titanium content, J. Mater. Res. Technol. 28 (2024) 967–979.
[42] J. Hou, S. Wu, C. Han, Q. Fu, Y. Cai, T. Wang, C. Chen, R. Wei, F. Li, Improving the strength of $Al_{0.3}$CoCrFeNi high-entropy alloy via induing dual-heterogeneous microstructure by aging treatment, Intermetallics 173 (2024) 108403.
[43] S. Niu, H. Kou, T. Guo, Y. Zhang, J. Wang, J. Li, Strengthening of nanoprecipitations in an annealed Al0.5CoCrFeNi high entropy alloy, Mater. Sci. Eng. A 671 (2016) 82–86.
[44] X. Shang, M.W. Fu, H. Zhang, J. Liu, X. Zhou, T. Ying, X. Zeng, Unraveling the transformation of ductile damage mechanisms of void evolution and strain localization based on deformation heterogeneity, Int. J. Plast. 171 (2023) 103785.
[45] A. Pineau, A.A. Benzerga, T. Pardoen, Failure of metals I: Brittle and ductile fracture, Acta Mater. 107 (2016) 424–483.
[46] Z.C. Luo, M.X. Huang, Revealing the Fracture Mechanism of Twinning-Induced Plasticity Steels, Steel Res. Int. 89 (2018) 1700433.
[47] Y. Luo, Q. Zheng, B. Sun, R. Sheng, J. Hou, Z. Chong, Q. Wang, Z. Guo, Z. Jia, Y. Tong, B. Shen, Phase-selective transformation enabled coherent interfaces for coordinated deformation in FCC-Laves eutectic high-entropy alloys, Mater. Sci. Eng. A 953 (2026) 149747.
[48] Y. Luo, Q. Wang, B. Sun, R. Sheng, Z. Guo, G. Zou, Z. Jia, Y. Tong, G. Sha, P. K. Liaw, B. Shen, Deformable Eutectic Alloy With Near-Theoretical Yield Strength via Hierarchical Nanoscale Multiphases and Sessile Defects, Adv. Sci. 13 (2026) e18764.
[49] Z. Chen, H. Xie, H. Yan, X. Pang, Y. Wang, G. Wu, L. Zhang, H. Tang, B. Gao, B. Yang, Y. Tian, H. Gou, G. Qin, Towards ultrastrong and ductile medium-entropy alloy through dual-phase ultrafine-grained architecture, J. Mater. Sci. Technol. 126 (2022) 228–236.
[50] G.W. Hu, L.C. Zeng, H. Du, Q. Wang, Z.T. Fan, X.W. Liu, Combined effects of solute drag and Zener pinning on grain growth of a NiCoCr medium-entropy alloy, Intermetallics 136 (2021) 107271.
[51] M. Alkayyali, M. Taghizadeh, F. Abdeljawad, Understanding grain boundary segregation and solute drag using computational and machine learning studies, Acta Mater. 275 (2024) 120037.
[52] Q. Wang, Z. Li, S. Pang, X. Li, C. Dong, P.K. Liaw, Coherent Precipitation and Strengthening in Compositionally Complex Alloys: A Review, Entropy 20 (2018) 878.
[53] Y. Zhang, R.B. Sills, Strengthening via Orowan Looping of Misfitting Plate-like Precipitates, J. Mech. Phys. Solids 173 (2023) 105234.
[54] T. Gladman, Precipitation hardening in metals, Mater. Sci. Technol. 15 (1999) 30–36.
[55] M. Wu, Z. Li, B. Gault, P. Munroe, I. Baker, The effects of carbon on the phase stability and mechanical properties of heat-treated FeNiMnCrAl high entropy alloys, Mater. Sci. Eng. A 748 (2019) 59–73.
[56] S. Zou, C. Dong, X. Tan, Z. Liang, W. Bao, B. He, W. Lu, Mitigating embrittlement of sigma phase in dual-phase high-entropy alloys through heterostructure design, Int. J. Plast. 187 (2025) 104272.
[57] X. Xu, Z. He, K. Zheng, L. Che, F. Zhao, D. Hua, Design of Fe-Co-Cr-Ni-Mn-Al-Ti Multi-Principal Element Alloys Based on Machine Learning, Materials (2026) 422.
[58] Q. Li, J.W. Mo, S.H. Ma, F.H. Duan, Y.L. Zhao, S.F. Liu, W.H. Liu, S.J. Zhao, C. T. Liu, P.K. Liaw, T. Yang, Defeating hydrogen-induced grain-boundary embrittlement via triggering unusual interfacial segregation in FeCrCoNi-type high-entropy alloys, Acta Mater. 241 (2022) 118410.
[59] B. Xiao, S. Liu, J. Zhang, Y. Zhou, Q. Li, J. Hou, W. Xiao, J. Zhang, Y. Zhao, C. T. Liu, L. Xu, T. Yang, Environmental embrittlement behavior of high-entropy alloys, Microstructures 3 (2023) 2023006.
[60] S. Guo, C. Ng, J. Lu, C.T. Liu, Effect of valence electron concentration on stability of fcc or bcc phase in high entropy alloys, J. Appl. Phys. 109 (2011) 103505.